FTIR and Resonance Raman Studies of Nitric Oxide Binding to H93G Cavity Mutants of Myoglobin†

Melissa R. Thomas,‡ Derek Brown,§ Stefan Franzen,§ and Steven G. Boxer*,‡

Department of Chemistry, Stanford University, Stanford, California 94305-5080, and Department of Chemistry, North Carolina State University, Raleigh, North Carolina 27695-8204

Received July 10, 2001; Revised Manuscript Received September 12, 2001

ABSTRACT: Nitric oxide (NO) binds to the myoglobin (Mb) cavity mutant, H93G, forming either a five- or six-coordinate Fe−NO complex. The H93G mutation eliminates the covalent attachment between the protein and the proximal ligand, allowing NO to bind H93G possibly from the proximal side of the heme rather than the typical diatomic binding pocket on the distal side. The question of whether NO binds on the distal or proximal side was addressed by FTIR spectroscopy of the N−O vibrational frequency $\bar{\nu}_{N-O}$ for a set of Mb mutants that perturb the electrostatic environment of the heme pocket. Vibrational spectra of five- and six-coordinate MbNO complexes indicate that $\bar{\nu}_{N-O}$ shifts (by as much as 26 cm^{-1}) to higher energies for the distal mutants H64V and H64V/H93G relative to the energies of wild-type and H93G MbNO, while $\bar{\nu}_{N-O}$ is not affected by the proximal side mutation S92A/H93G. This result suggests that NO binds on the distal side of heme in the five- and six-coordinate MbNO complexes of H93G. Additionally, values of the Fe−NO vibrational frequency $\bar{\nu}_{Fe-NO}$ as measured by resonance Raman spectroscopy are reported for the distal and proximal double mutants of H93G. These results suggest that $\bar{\nu}_{Fe-NO}$ is not very sensitive to mutations that perturb the electrostatic environment of the heme pocket, leading to the observation that $\bar{\nu}_{N-O}$ and $\bar{\nu}_{Fe-NO}$ are not quantitatively correlated for the MbNO complexes presented here. Furthermore, $\bar{\nu}_{N-O}$ and $\bar{\nu}_{Fe-NO}$ do not correlate well with equilibrium constants for imidazole binding to the five-coordinate MbNO complexes of the H93G double mutants. The data presented here do not appear to support the presence of π-back-bonding or an inverse *trans* effect of NO binding in Mb mutants that alter the electrostatic environment of the heme pocket.

When nitric oxide (NO)[1] binds to heme proteins, it is believed to exert a repulsive *trans* effect that weakens or breaks the *trans* axial bond with important functional consequences. For example, native myoglobin (Mb) (*1*, *2*) and the β-chains of hemoglobin (*3*, *4*) form six-coordinate NO complexes, where the proximal bond is weakened, but not broken, while the α-chains of hemoglobin (*3*−*5*) and guanylate cyclase (*6*−*9*) form five-coordinate complexes upon addition of NO. The factors that govern the *trans* effect, and whether the axial bond ruptures or is only weakened in a particular protein environment, are not clear and are central to understanding how NO exerts its physiological function. By definition, the inverse *trans* effect implies that the His−Fe and Fe−NO bond strengths would be anticorrelated. Furthermore, possible π-back-bonding within the heme Fe−NO complex would lead to an anticorrelation between the Fe−NO and N−O bonds and a positive correlation between the His−Fe and N−O bonds. Several studies have attempted to establish such relationships between the His−Fe, Fe−NO, and N−O bonds in protein and model Fe−NO complexes (*10*, *11*).

The myoglobin cavity mutant H93G offers an interesting protein-based model system for the systematic investigation of heme NO complexes. In H93G, the proximal histidine that ligates the iron has been substituted with glycine, generating a cavity adjacent to the iron (*12*). This cavity can be filled with exogenous organic ligands such as imidazole that ligate the iron, thereby mimicking the histidine side chain and restoring properties that are similar, but not identical, to those of the wild type (WT). In particular, nitric oxide binds wild-type Mb on the distal side of the heme, generating a six-coordinate complex with NO and the proximal histidine as axial ligands. In contrast, when nitric oxide binds the cavity mutant in the presence of a relatively low concentration of exogenous imidazole (or other organic ligands), the

† This work is supported in part by Grant GM27738 from the National Institutes of Health to S.G.B. M.R.T. was the recipient of a NSF Predoctoral Fellowship.

* To whom correspondence should be addressed. E-mail: Sboxer@stanford.edu. Phone: (650) 723-4482. Fax: (650) 723-4817.

‡ Stanford University.

§ North Carolina State University.

[1] Abbreviations: NO, nitric oxide; Mb, myoglobin; WT, wild-type; SW, sperm whale; Hb, hemoglobin; sGC, soluble guanylate cyclase; CO, carbon monoxide; MbNO, nitrosylmyoglobin; MbCO, carbonmonoxymyoglobin; met CN Mb, metcyanomyoglobin; met H_2O Mb, Fe(III) Mb with H_2O as an axial ligand; Im, imidazole; H93G(Im), myoglobin cavity mutant H93G with Im incorporated as an axial ligand; H93G−NO, five-coordinate complex of NO bound to H93G Mb; H93G(Im)NO, six-coordinate complex of NO bound to H93G(Im) Mb; H64V/H93G, distal electrostatic/H93G Mb double mutant; V68L/H93G, distal electrostatic/H93G Mb double mutant; S92A/H93G, proximal electrostatic/H93G Mb double mutant; $\bar{\nu}_{N-O}$, N−O stretching frequency; $\bar{\nu}_{Fe-NO}$, Fe−NO stretching frequency; $\bar{\nu}_{C-O}$, C−O stretching frequency; K_{Im}, equilibrium binding constant for association of imidazole with five-coordinate H93G−NO single and double mutants; FTIR, Fourier transform infrared spectroscopy; NMR, nuclear magnetic resonance; EPR, electron paramagnetic resonance; MCD, magnetic circular dichroism; $\Delta\mu$, Stark tuning rate.

10.1021/bi011440l CCC: $20.00
Published on Web 11/15/2001

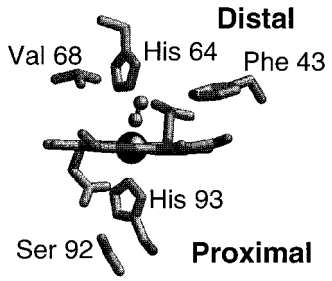

FIGURE 1: Representation of the heme pocket of wild-type sperm whale MbNO depicting the proximal amino acids, His 93 and Ser 92, and the distal amino acids, His 64 and Val 68.

exogenous imidazole−iron bond breaks, and a five-coordinate complex, denoted H93G−NO, forms (*13*). The coordination states have been characterized in considerable detail by absorption, EPR (*13*), and MCD spectroscopy (*14*, *15*). At a high relative imidazole concentration, a six-coordinate Fe−NO heme complex, termed H93G(Im)NO, is formed. Thus, this system has features of both five- and six-coordinate NO heme complexes. Although it is tempting to assume that NO is in the distal pocket in the H93G−NO five-coordinate complex, without a proximal ligand covalently linked to the protein, it could bind on either the distal side or the proximal side of the heme iron. A related question arises in general for H93G as the distal and proximal pockets are no longer defined by the proximal linkage to the protein backbone. In the case of met H_2O H93G(Im), the X-ray structure unambiguously shows that the exogenous Im is in the proximal cavity (*16*); this has likewise been demonstrated in solution for the met CN and CO forms by extensive proton NMR measurements (*17*, *18*). In recent work in our lab, we used ^{19}F NMR spectroscopy to demonstrate that NO is bound on the distal side of heme in the five- and six-coordinate MbNO complexes of H93G. For these experiments, a unique cysteine residue was incorporated on either the distal or proximal side of heme as an attachment site for the fluorine NMR probe (*19*).

An alternative strategy for determining the side on which NO binds in H93G−NO would be to use the N−O vibrational frequency $\bar{\nu}_{N-O}$ as measured by FTIR spectroscopy. It has been shown that the NO stretching frequency is highly sensitive to mutations in neighboring amino acids in the distal pocket of myoglobin, particularly mutations that introduce or remove charged residues or affect hydrogen bonding in the pocket. Introduction of the electrostatic mutations V68D and V68N causes the NO stretching frequency to shift by +17 and −31 cm^{-1}, respectively (*20*). Moreover, replacement of the distal histidine with a nonpolar residue in H64V causes $\bar{\nu}_{N-O}$ to increase by 26 cm^{-1} (*20*). Introduction of similar electrostatic or hydrogen bonding changes on the distal and proximal sides of heme in H93G Mb is predicted to cause greater shifts in $\bar{\nu}_{N-O}$ for mutations in nearby residues (Figure 1). More specifically, distal electrostatic mutations should primarily affect NO bound only on the distal side, while proximal electrostatic mutations are expected to affect the stretching frequency of NO if it is bound on the proximal side. A similar strategy used FTIR and ^1H NMR spectroscopies to confirm that CO binds on the distal side of heme in imidazole-free preparations of H93G−CO (*21*). Results of FTIR experiments are discussed below and are consistent with NO binding on the distal side of heme in both five- and six-coordinate NO complexes of H93G. Additionally, Fe−NO vibrational frequencies $\bar{\nu}_{Fe-NO}$ are reported for H93G electrostatic double mutants as measured by resonance Raman spectroscopy. Implications for the π-back-bonding and *trans* effect of NO binding will be discussed in light of the vibrational data as well as the affinities for imidazole binding to the five-coordinate MbNO complexes of the H93G variants.

MATERIALS AND METHODS

Protein Preparation. Wild-type sperm whale myoglobin and the H93G, H64V, V68L, H64V/H93G, S92A/H93G, and V68L/H93G variants were expressed and purified from *Escherichia coli* as described previously (*12*, *17*, *22*). Protein solutions were concentrated to ∼4 mM in a 50/50 d_3-glycerol/buffer [100 mM phosphate buffer in D_2O (pH 7, uncorrected for deuterium)] mixture. Solutions of the six-coordinate H93G single and double mutants also contained at least 10 mM imidazole. H64V/H93G and S92A/H93G samples required as much as 400 mM imidazole for generation of six-coordinate MbNO complexes. V68L single and double mutants were also prepared in two additional buffers: 100 mM citrate buffer in D_2O (pH 5.3) and 25 mM borate buffer in D_2O (pH 9.0) (pHs uncorrected for deuterium). Concentrated protein samples were purged with N_2 gas to remove oxygen, and reduced with ∼3 equiv of 1 M sodium dithionite in D_2O. Samples were immediately exposed to NO that had been bubbled through 0.5 M potassium hydroxide (^{14}NO, natural abundance, Matheson; ^{15}NO, 99% isotopic purity, Isotec). Alternatively, ^{15}NO-bound Mb was formed by the in situ generation of ^{15}NO from the reaction of ∼10 equiv of 1 M sodium [^{15}N]nitrite in D_2O with excess sodium dithionite in the sample ^{15}N-nitrite (*23*). Formation of the MbNO complexes was confirmed by monitoring the UV−vis absorption spectra.

Photolysis Difference FTIR Spectroscopy. Photolysis difference FTIR spectra were obtained using a Bruker IFS 66V/S FTIR spectrometer (2 cm^{-1} resolution) using an MCT detector. Protein samples were injected into an IR cell consisting of CaF_2 windows separated by an ∼25 μm Teflon spacer. Samples were attached to the coldfinger of a continuous-flow liquid helium cryostat and cooled to ∼7 K. Spectra were measured at 7 K before, during, and after photolysis of bound NO with a 600 W halogen bulb. An IR filter was placed between the photolysis light source and the sample to prevent heating of the sample during photolysis. The photolysis difference spectrum [ΔA (photolyzed minus unphotolyzed)] gives the spectrum of the NO ligand bound to Mb, because the photolyzed NO can be trapped unbound to the heme iron at 7 K. The NO stretching frequency for each protein was confirmed by ^{15}NO isotope substitution.

Resonance Raman Spectroscopy. Resonance Raman spectra were obtained by exciting the edge of the Soret band at 441 nm using a helium−cadmium laser (LiConix, model 4250/10NF-R000) for six-coordinate MbNO samples. Alternatively, the Soret band of five-coordinate MbNO was excited at 419 nm using a Coherent 700 dye laser operated with Stilbene 420 dye and pumped with the tripled output of a mode-locked Antares 76-YAG laser (Coherent). The dye laser output was calibrated using Rayleigh scattering, toluene and carbon tetrachloride standards, and lines from

Kr and Ar lamps. Beams from either laser were collimated and cylindrically focused to a vertical line of ~0.5 mm and typically 20−35 mW at the sample. Raman scattered light passed through a Spex 1877 Triplemate monochromator and was detected by a liquid N_2-cooled CCD camera (ISA Spex, model CCD-3000). Protein samples were prepared by in situ generation of either ^{14}NO or ^{15}NO using the sodium dithionite/sodium nitrite method in 100 mM phosphate buffer (pH 7) as described above. Solutions of the six-coordinate H93G single and double mutants also contained at least 10 mM imidazole, as indicated above. Samples with identical concentrations (typically, 1−2 mM Mb) and volumes (typically, 65−80 μL) were prepared simultaneously as both Mb^{14}NO and Mb^{15}NO for each protein. Samples were injected into sealed, N_2-purged NMR tubes and spun with an air piston spinning sample holder (Princeton Photonics, model Raman 101). Spectra were measured at room temperature for two to eight acquisitions with exposure times of 20−200 s, alternating between Mb^{14}NO and Mb^{15}NO to minimize sample degradation. Each sample scan was repeated four to eight times to improve the signal-to-noise ratio.

Titration of Five-Coordinate MbNO Samples with Imidazole. Equilibrium binding constants for imidazole binding to the five-coordinate NO complexes of H93G, H64V/H93G, S92A/H93G, and V68L/H93G were determined by titration with imidazole (*24*). Concentrated solutions of the five-coordinate NO complexes were prepared as described above. Protein solutions were diluted to ~2 μM in sealed, anaerobic quartz cuvettes containing 100 mM sodium phosphate buffer (pH 7). Titrations were carried out by injecting aliquots of 1 M imidazole (pH 7) into the samples, and were monitored by changes in the Soret region of the UV−vis absorption spectra obtained using a Perkin-Elmer Lambda 12 UV−vis spectrometer.

RESULTS

IR Spectra of the N−O Stretch. The photolysis difference spectra of wild-type, H64V, H93G, H64V/H93G, and S92A/H93G five- and six-coordinate MbNO complexes are shown in Figure 2. Spectra were measured for both ^{14}NO- and ^{15}NO-bound samples to assign the bands associated with the N−O stretch. All NO bands exhibit an isotope shift of ~30 cm^{-1}, a magnitude that agrees with reduced mass calculations for ^{14}NO compared to ^{15}NO assuming that NO is an isolated oscillator (*25*). Additional bands that do not shift upon isotope substitution are visible in the spectra. These bands are attributed to small changes that occur in the protein structure upon photolysis, and most likely arise from the nearby protein amide I (1655 cm^{-1}) and amide II (1555 cm^{-1}) bands. The NO band splits into two peaks when it absorbs near 1585 cm^{-1}, as seen in the wild-type, H93G(Im), and S92A/H93G(Im) Mb^{15}NO spectra. This phenomenon has been explained previously as a Fermi resonance that occurs between the NO stretching frequency and a C_β−C_β stretch (ν_2) in the heme at 1583 cm^{-1} (*11*, *20*). This splitting does not occur unless $\bar{\nu}_{N-O}$ is close to this value. The ^{14}NO and ^{15}NO stretching frequencies for each protein are summarized in Table 1.

The photolysis difference spectra of six-coordinate V68L−NO and V68L/H93G(Im)NO complexes at pH 5.3 and 9.0, as well as five-coordinate V68L/H93G−NO at pH 7, are shown in Figure 3. Spectra for the V68L variants are cluttered with multiple bands, particularly at pH 7 (data not shown). Each V68L variant appears to have three NO bands identified by isotope substitution. These bands overlap quite closely with protein bands that change upon photolysis but do not

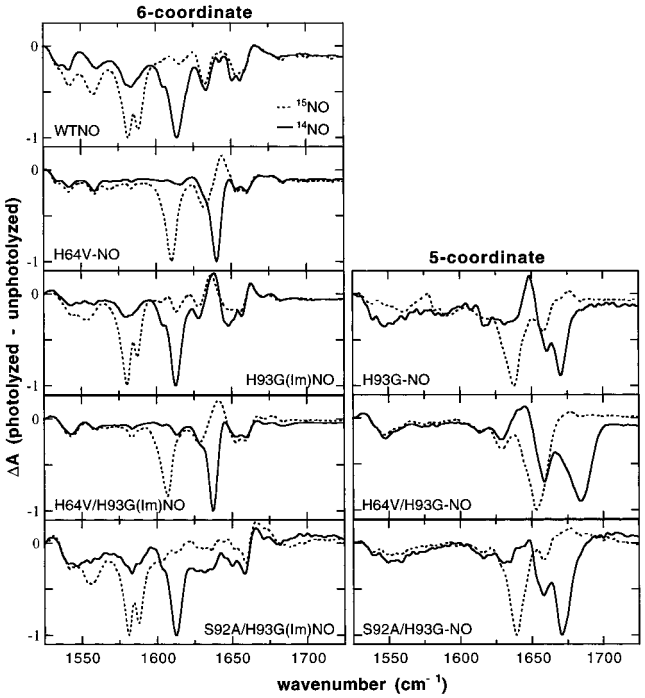

FIGURE 2: FTIR photolysis difference spectra (photolyzed minus unphotolyzed) of MbNO at 7 K for the indicated Mb variants. Spectra for six-coordinate MbNO samples are shown on the left, while spectra for five-coordinate MbNO samples are in the right column. Protein concentrations were ~4 mM in a 50/50 d_3-glycerol/phosphate buffer mixture in D_2O (pH 7, uncorrected for deuterium). The spectra are normalized for the unit absorbance difference at the maximum of the difference spectrum (the actual difference ΔA was typically ≈0.005−0.01). The solid lines are difference spectra for Mb^{14}NO; the dashed lines are for Mb^{15}NO. When $\bar{\nu}_{N-O}$ occurs near 1585 cm^{-1}, a Fermi resonance splits the band (see the text).

Table 1: $\bar{\nu}_{N-O}$ for MbNO Variants As Measured by FTIR[a]

protein	coordination[b] number	$\bar{\nu}^{14}_{N-O}$ (cm^{-1})	$\bar{\nu}^{15}_{N-O}$ (cm^{-1})
wild-type MbNO	6	1614	1581, 1588[c]
H64V−NO	6	1640	1610
H93G(Im)NO	6	1613	1580, 1587[c]
H93G−NO	5	1670	1638
H64V/H93G(Im)NO	6	1637	1607
H64V/H93G−NO	5	1684	1653
S92A/H93G(Im)NO	6	1613	1581, 1588[c]
S92A/H93G−NO	5	1671	1639
V68L−NO, pH 9[d]	6	1575, 1604	1546, 1574
V68L−NO, pH 5.3[d]	6	1576, 1603, **1621**	1550, 1572, **1592**
V68L/H93G(Im)NO, pH 9[d]	6	1573, 1604	1546, 1575
V68L/H93G(Im)NO, pH 5.3[d]	6	1603, **1620**	**1589**, 1646
V68L/H93G−NO[d]	5	**1619**, 1670	1590, **1643**

[a] Data are reported for protein samples at pH 7, unless otherwise stated. [b] The MbNO complex is a six-coordinate His−Fe−NO, six-coordinate Im−Fe−NO, or five-coordinate Fe−NO complex. [c] The peak is split into two peaks near 1585 cm^{-1} due to a Fermi resonance with a porphyrin mode; see the text. [d] V68L single and double mutants exhibit multiple, pH-dependent bands due to protonation substates; see the text. The major peak is listed in bold type.

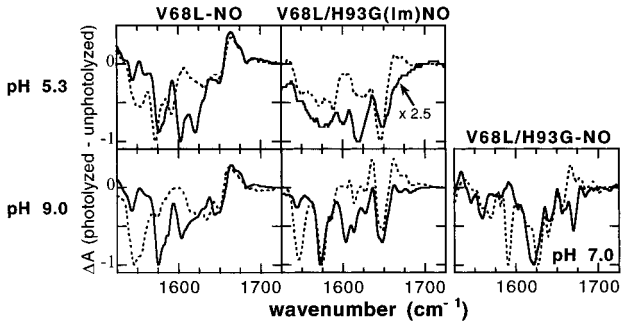

FIGURE 3: FTIR photolysis difference spectra (photolyzed minus unphotolyzed) of MbNO at 7 K for V68L variants: (top left panel) V68L−NO at pH 5.3, (bottom left panel) V68L−NO at pH 9.0, (top center panel) six-coordinate V68L/H93G(Im)NO at pH 5.3, (bottom center panel) six-coordinate V68L/H93G(Im)NO at pH 9.0, and (bottom right panel) five-coordinate V68L/H93G−NO at pH 7.0. Protein concentrations were ~4 mM in a 50/50 d_3-glycerol/phosphate buffer mixture in D_2O (pH 7, uncorrected for deuterium). The spectra are normalized for the unit absorbance difference at the maximum of the difference spectrum (the actual difference ΔA was typically ≈0.001). The solid lines are difference spectra for $Mb^{14}NO$; the dashed lines are for $Mb^{15}NO$.

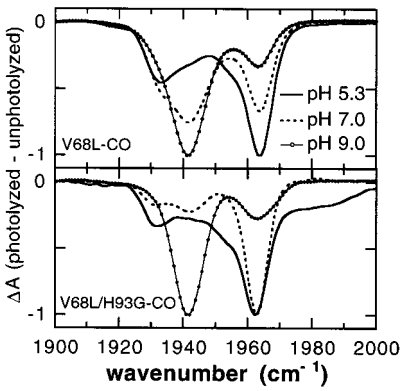

FIGURE 4: FTIR photolysis difference spectra (photolyzed minus unphotolyzed) of MbCO at 7 K for V68L (top panel) and V68L/H93G(Im) Mb (bottom panel). Difference spectra are shown for MbCO at pH 5.3 (solid lines), 7.0 (dashed lines), and 9.0 (dotted solid lines). Protein concentrations were ~4 mM in a 50/50 d_3-glycerol/phosphate buffer mixture in D_2O. The spectra are normalized for the unit absorbance difference at the maximum of the difference spectrum (the actual difference ΔA was typically ≈0.01).

exhibit an isotope shift. Spectra were obtained for V68L single and double mutants at pH 5.3 and 9.0 in an attempt to identify the observed isotope-sensitive bands. FTIR photolysis difference spectra of V68L−NO reveal the bands at 1575 and 1604 cm^{-1} to be present at both pH 5.3 and 9.0, while the band at 1621 cm^{-1} is only present at low pH. Spectra for six-coordinate V68L/H93G(Im)NO at pH 9.0 closely resemble that of V68L−NO at pH 9.0, suggesting that $\bar{\nu}_{N-O}$ exhibits a similar pH dependence in the V68L single and double mutants. The V68L/H93G double mutant is apparently much more sensitive to acidic solutions than the V68L single mutant, and was observed to precipitate extensively upon dialysis into pH 5.3 buffer. As a result, FTIR spectra for ^{14}NO- and ^{15}NO-bound V68L/H93G(Im) were of lower intensity (typically, $\Delta A \approx 0.0003-0.0008$) and more difficult to resolve. The five-coordinate V68L/H93G−NO species is less stable than six-coordinate V68L/H93G(Im)NO, and could not be prepared at pH 5.3 or 9.0, preventing the acquisition of five-coordinate V68L/H93G−NO spectra at pH 5.3 or 9.0. Assignments of $\bar{\nu}_{N-O}$ bands for six-coordinate V68L/H93G(Im)NO were made by comparison with the V68L single mutant. Possible origins of the three bands observed for V68L variants will be discussed further below.

IR Spectra of the C−O Stretch. In an attempt to elucidate the origin of the three NO bands observed in V68L variants, C−O stretching frequencies $\bar{\nu}_{C-O}$ were measured for V68L- and V68L/H93G(Im) MbCO. MbCO samples were prepared in a manner identical to that of the MbNO samples, with the exception that samples were exposed to CO gas (Matheson) instead of NO gas. Photolysis difference spectra were obtained for MbCO samples following the procedure described above for MbNO samples. The photolysis difference spectra of V68L−CO and V68L/H93G(Im)CO samples at pH 5.3, 7.0, and 9.0 are shown in Figure 4, and $\bar{\nu}_{C-O}$ values are summarized in Table 2. The C−O stretching mode has been studied extensively for a variety of mutants. Typical spectra of MbCO exhibit one or more of three CO bands classified as A_0, A_1, and A_2 states, corresponding to various protonation substates of the distal pocket residues (*26*). The

Table 2: $\bar{\nu}_{C-O}$ for V68L Variants of MbCO As Measured by FTIR

protein	pH	$\bar{\nu}_{C-O}$ (cm^{-1})[a]
V68L−CO	9	**1941**, 1963
V68L−CO	5.3	1933, **1964**
V68L/H93G(Im)CO	9	**1942**, 1963
V68L/H93G(Im)CO	5.3	1931, **1962**
H93G(Im)CO[b]	7	**1946**, 1965
wild-type MbCO[c]	7	1945

[a] Peak positions commonly denoted as the A_0, A_1, and A_2 substates; see the text. Major peak positions are listed in bold type. [b] Data taken from ref *21*. [c] Data taken from ref *39*. Wild-type MbCO at pH 5.3 has a second band at 1965 cm^{-1} (A_0).

spectrum of H93G(Im)CO is quite similar to that of wild-type MbCO (*18*). In contrast, the CO photolysis spectra of V68L and V68L/H93G(Im) differ dramatically from those of wild-type and H93G(Im) MbCO. The A_1 substate of wild-type and H93G(Im) MbCO (1945 cm^{-1}) is apparent for samples at pH 7.0, while spectra for the V68L and V68L/H93G(Im) MbCO samples are not dominated by the A_1 substate until the pH is increased to 9.0. For comparison, absorption spectra are shown in Figure 5 for WT and V68L MbCO samples at 295 K. Samples were prepared in a manner identical to that for the compounds used for photolysis difference spectroscopy at 7 K, in a 50/50 d_3-glycerol/buffer [100 mM phosphate buffer in D_2O (pH 7, uncorrected for deuterium)] mixture. Room-temperature spectra were corrected for solvent absorption, using a reference sample of a 50/50 d_3-glycerol/buffer mixture in D_2O. The room-temperature data presented here are consistent with $\bar{\nu}_{C-O}$ values reported earlier for V68L at 295 K (*27*). Differences between the room-temperature absorption and cryogenic photolysis difference spectra of V68L MbCO are quite striking, particularly in comparison with the spectra of wild-type MbCO as discussed below.

Resonance Raman Spectra of the Fe−NO Vibration. The low-frequency region of the resonance Raman spectra and corresponding isotope difference spectra are shown in Figure 6 for ^{14}NO- and ^{15}NO-bound Mb variants. Spectra for six-coordinate MbNO are shown in columns on the left side of Figure 6, while those for five-coordinate MbNO are shown

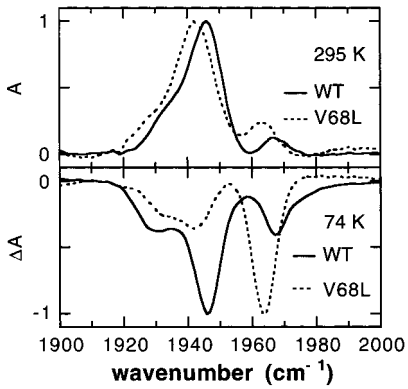

FIGURE 5: FTIR spectra of wild-type and V68L MbCO at 295 and 74 K. (Top) Absorption spectra are shown for wild-type (solid line) and V68L MbCO (dashed line) at 295 K. (Bottom) Photolysis difference spectra (photolyzed minus unphotolyzed) of wild-type (solid line) and V68L MbCO (dashed line) at 74 K. Photolysis difference spectra were obtained using a pumped, liquid N_2 immersion cryostat at 74 K (*40*). Protein concentrations were ~4 mM in a 50/50 d_3-glycerol/buffer mixture [100 mM phosphate buffer in D_2O (pH 7, uncorrected for deuterium)]. The spectra are normalized for the unit absorbance or absorbance difference at the maximum of the MbCO spectrum (the actual intensity A or ΔA was typically ≈0.01).

on the right. Resonance Raman spectra for five- and six-coordinate H93G, H64V/H93G, and S92A/H93G samples contained a broad fluorescence background that did not affect the resonance Raman isotope difference spectra. Adjacent to each resonance Raman spectrum is the corresponding isotope difference spectrum ($Mb^{14}NO$ minus $Mb^{15}NO$) for each protein, depicted as individual data points. Observed $\bar{\nu}_{Fe-NO}$ values for each mutant exhibit an isotope shift of ~14 cm^{-1}, a value that is consistent with isotope differences calculated from crystallography data for Fe−N−O bonds in wild-type MbNO (*11*). To determine values for $\bar{\nu}_{Fe-^{14}NO}$ and $\bar{\nu}_{Fe-^{15}NO}$, the isotope difference spectra are fit with a function consisting of a sum of two Gaussian curves (depicted as a solid line in each resonance Raman difference spectrum). The ^{14}NO- and ^{15}NO-bound samples were prepared with exactly matched concentrations, and the data for successive pairs of samples were normalized to the sample concentration. Peak maxima obtained from fitting the resonance Raman isotope difference spectra are listed in Table 3 for the five- and six-coordinate MbNO complexes of the wild type, H64V, V68L, H93G, H64V/H93G, S92A/H93G, and V68L/H93G.

Values of $\bar{\nu}_{Fe-^{14}NO}$ obtained for the five-coordinate MbNO complexes of H93G, H64V/H93G, S92A/H93G, and V68L/H93G are essentially identical (clustering around 533−535 cm^{-1}). Frequencies for the six-coordinate $Mb^{14}NO$ complexes vary from 553 to 562 cm^{-1}. The spectra presented here are consistent with low-frequency resonance Raman data reported previously for sperm whale wild-type $Mb^{14}NO$ (*11*). Values for $\bar{\nu}_{Fe-NO}$ were reported previously as 560 cm^{-1} for the observed isotope difference spectrum, and as 552 cm^{-1} for isotope difference data fit to a Gaussian model. In cases where the bandwidth is larger than the isotope difference, Tomita and co-workers found it necessary to fit difference spectra with a Gaussian model to determine band positions. Five-coordinate MbNO data were reported earlier to be 524 cm^{-1} for sperm whale wild-type $Mb^{14}NO$ at pH 4, in which His 93 is protonated and the proximal His−Fe bond is cleaved (*11*). All of the H93G double mutants presented here exhibit $\bar{\nu}_{Fe-NO}$ values that are slightly higher (2−8 cm^{-1}) than that for wild-type MbNO. The highest $\bar{\nu}_{Fe-NO}$ was observed for six-coordinate H93G(Im)NO. Spectra for the distal mutant V68L and wild-type MbNO are essentially identical, while $\bar{\nu}_{Fe-NO}$ for H64V is ~3 cm^{-1} higher than that of the wild type. In contrast, values for the six-coordinate double mutants H64V/H93G and V68L/H93G are both ~3 cm^{-1} lower than that for H93G(Im)NO. Additionally, $\bar{\nu}_{Fe-NO}$ for six-coordinate S92A/H93G is 6 cm^{-1} lower than that for H93G(Im)NO. Differences in $\bar{\nu}_{Fe-NO}$ observed for six-coordinate double mutants are largely eliminated in the corresponding five-coordinate MbNO samples.

Binding of Imidazole to Five-Coordinate MbNO Complexes. Five-coordinate complexes of NO bound to H93G Mb variants are formed in the absence of exogenous imidazole, and are characterized by a broad Soret band at 400 nm. Addition of excess imidazole to the five-coordinate NO complex generates a six-coordinate MbNO complex, causing the Soret band to shift from 400 to 420 nm. Titration of the five-coordinate MbNO complex with imidazole enables the determination of equilibrium constants for the binding of imidazole to the five-coordinate H93G−NO single and double mutants, as described previously (*24*). Plotting the change in absorbance at 420 nm (ΔA_{420}) versus the ratio of ΔA_{420} to the imidazole concentration results in a straight line with a slope equal to $-1/K_{Im}$. Equilibrium binding constants measured for imidazole binding to five-coordinate MbNO complexes of H93G, H64V/H93G, S92A/H93G, and V68L/H93G are summarized in Table 4. Imidazole affinities for H93G−NO and V68L/H93G−NO are quite similar, but imidazole binding to H64V/H93G−NO and S92A/H93G−NO is weaker by factors of ~45 and ~150, respectively.

DISCUSSION

NO binds on the distal side in H93G−NO mutants: variations in $\bar{\nu}_{N-O}$ for wild-type, H64V, H93G(Im), H64V/H93G(Im), and S92A/H93G(Im) six-coordinate MbNO samples reflect the effect of changes in the electrostatic environment in the vicinity of the N−O oscillator. The N−O stretching frequency responds to changes in the electrostatic field caused by mutations near the heme, shifting by an internal Stark effect (*20*, *28*). As summarized in Figure 2 and Table 1, values for $\bar{\nu}_{N-O}$ are virtually identical for wild type, H93G(Im), and S92A/H93G(Im). In contrast, the H64V mutation causes $\bar{\nu}_{N-O}$ to shift to higher energy by 26 cm^{-1} compared to that of wild-type MbNO. Likewise, the H64V/H93G(Im)NO spectrum shows a 24 cm^{-1} shift to higher energy compared with $\bar{\nu}_{N-O}$ measured for H93G(Im)-NO. The observation of a similar shift in $\bar{\nu}_{N-O}$ for the double mutant H64V/H93G(Im)NO suggests that the change in the distal electrostatic environment due to the H64V mutation is sensed by the bound NO. For NO to be close enough to be affected by the H64V mutation, it must be bound on the distal side of the heme. Furthermore, the S92A mutation changes the proximal pocket environment by removing a potential hydrogen bonding interaction with the hydroxyl group of the serine side chain (*24*). This mutation should not affect $\bar{\nu}_{N-O}$ for NO bound on the distal side. The absence of an observed effect of the S92A mutation on the N−O stretch of six-coordinate S92A/H93G(Im)NO further bolsters

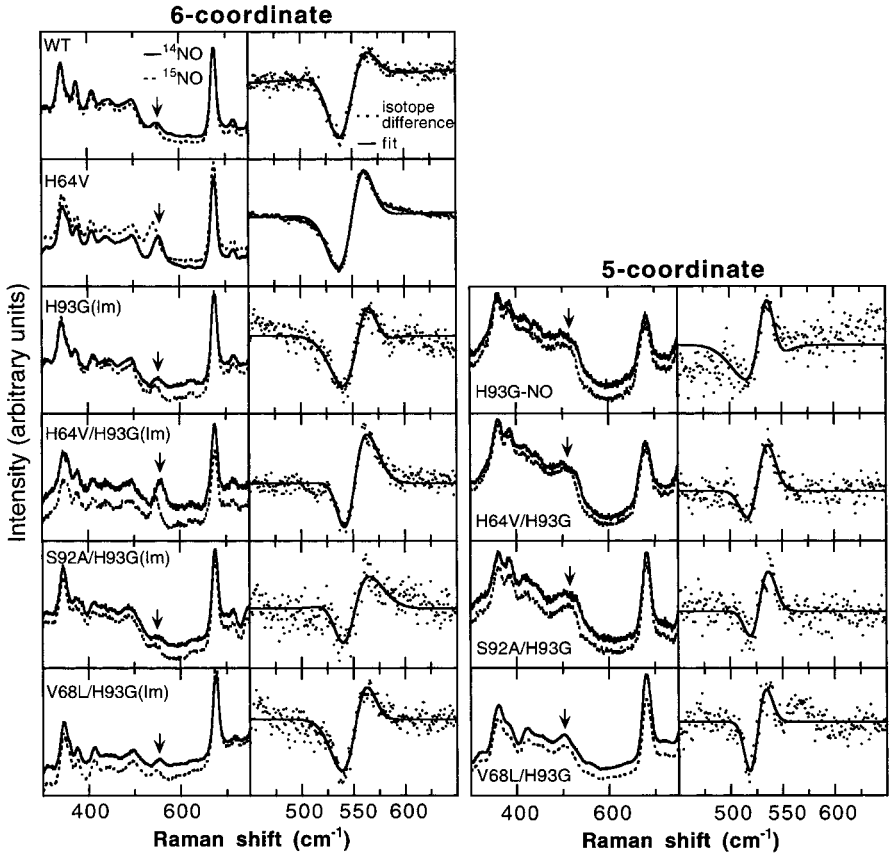

FIGURE 6: Resonance Raman spectra and isotope difference spectra ($Mb^{14}NO$ minus $Mb^{15}NO$) for the indicated MbNO variants. Spectra are arranged in columns from left to right as follows: six-coordinate $Mb^{14}NO$ and $Mb^{15}NO$ spectra, six-coordinate MbNO isotope difference spectra, five-coordinate $Mb^{14}NO$ and $Mb^{15}NO$ spectra, and five-coordinate MbNO isotope difference spectra. Protein concentrations were ~1−2 mM in 100 mM phosphate buffer (pH 7). Raman spectra are shown for $Mb^{14}NO$ (solid lines) and $Mb^{15}NO$ (dotted lines). Isotope difference spectra (represented as points) are fit with a sum of two Gaussian curves (solid lines). To facilitate comparison with other spectra, the unsubtracted $Mb^{14}NO$ and $Mb^{15}NO$ spectra of H93G, H64V/H93G, and S92A/H93G were corrected for a broad fluorescence background.

Table 3: $\bar{\nu}_{Fe-NO}$ for MbNO Variants As Measured by Resonance Raman[a]

protein[b]	coordination[c]	$\bar{\nu}_{Fe-^{14}NO}$ (cm^{-1})	$\bar{\nu}_{Fe-^{15}NO}$ (cm^{-1})
wild-type MbNO	6	554	540
H64V−NO	6	557	544
H93G(Im)NO	6	562	548
H93G−NO	5	535	521
H64V/H93G(Im)NO	6	559	544
H64V/H93G−NO	5	534	520
S92A/H93G(Im)NO	6	556	542
S92A/H93G−NO	5	535	521
V68L−NO	6	553	539
V68L/H93G(Im)NO	6	559	545
V68L/H93G−NO	5	533	519

[a] Frequencies are peak maxima obtained from fitting the resonance Raman isotope difference spectra with a sum of two Gaussian curves; see the text. [b] Data are reported for protein samples at pH 7. [c] The MbNO complex is a six-coordinate His−Fe−NO, six-coordinate Im−Fe−NO, or five-coordinate Fe−NO complex.

Table 4: Titration Data for Imidazole Binding to Five-Coordinate MbNO Variants[a]

protein	K_{Im}[b]	protein	K_{Im}[b]
H93G−NO[c]	1500 ± 100	S92A/H93G−NO[d]	10 ± 5
H64V/H93G−NO	32 ± 6	V68L/H93G−NO	1600 ± 170

[a] Titration data measured by the change in the Soret band of UV−vis absorption spectra. [b] Equilibrium binding constant for imidazole binding to the five-coordinate NO complex: H93G−NO + Im ⇌ H93G(Im)NO, where K_{Im} = [H93G(Im)NO]/([H93G−NO][Im]). Tabulated values represent association constants. [c] Data taken from ref *13*. [d] Data taken from ref *24*.

the assertion that NO binds on the distal side in six-coordinate H93G(Im)NO.

An analogous effect of the distal and proximal mutations on $\bar{\nu}_{N-O}$ is expected for the five-coordinate H93G−NO single and double mutants. As summarized in Figure 2 and Table 1, values for $\bar{\nu}_{N-O}$ are also quite similar for the five-coordinate NO complexes of H93G and S92A/H93G. The value of $\bar{\nu}_{N-O}$ measured for the five-coordinate H93G−NO sample is consistent with that measured for five-coordinate NO complexes of porphyrin model compounds, such as octaethylporphyrin in benzene ($\bar{\nu}_{N-O}$ = 1669 cm^{-1}) (*10*). As in the six-coordinate case, the H64V mutation causes the N−O stretching frequency to shift to higher energy in the five-coordinate NO complex of H64V/H93G. The magnitude of the shift in $\bar{\nu}_{N-O}$ is lower (+16 cm^{-1}) for H64V/H93G−NO than for six-coordinate H64V/H93G(Im)NO (+24 cm^{-1}). This mitigated effect of the H64V mutation on the five-coordinate complex may be attributed to subtle differences in bonding or electronic structure between the five- and six-coordinate species. Structural differences between five- and six-coordinate H93G−NO might alter the projection of the electrostatic field onto the N−O bond, thereby causing different magnitudes of the shift in $\bar{\nu}_{N-O}$ due to the H64V

mutation. Regardless of this point, the change in $\bar{\nu}_{N-O}$ due to the distal H64V mutation in addition to the lack of an effect of the S92A mutation on $\bar{\nu}_{N-O}$ suggests that NO is bound on the distal side of heme in five-coordinate H93G−NO, a result that is consistent with ^{19}F NMR data using fluorine-labeled surface probes (*19*). In summary, the FTIR data for the N−O stretch indicate that NO binds on the distal side of heme in both the five- and six-coordinate NO complexes of the Mb cavity mutant, H93G.

Resonance Raman Spectra of $\bar{\nu}_{Fe-NO}$ in MbNO Complexes. Resonance Raman isotope difference spectra allow for the determination of $\bar{\nu}_{Fe-NO}$ for MbNO. Spectra obtained for the six-coordinate MbNO variants presented in this paper are consistent with published spectra of wild-type sperm whale MbNO. Values obtained for five-coordinate MbNO complexes of H93G single and double mutants are ∼10 cm^{-1} higher than values reported for five-coordinate wild-type MbNO generated by protonation of the proximal His 93 residue (*11*). However, the acidic form of wild-type MbNO is fundamentally different from H93G−NO at pH 7, even though both proteins are five-coordinate complexes. At pH 4, both the proximal His 93 and distal His 64 side chains of wild-type Mb are protonated, whereas in five-coordinate H93G−NO at pH 7, His 93 is absent and His 64 is not protonated. This difference could explain the variation in $\bar{\nu}_{Fe-NO}$ for five-coordinate H93G−NO at pH 7 compared with wild-type MbNO at pH 4. An analogous effect is observed for $\bar{\nu}_{Fe-NO}$ of wild-type MbCO at pH 4 compared with that at pH 7. Protonation of the distal histidine causes $\bar{\nu}_{Fe-NO}$ to shift to lower energy (488 cm^{-1}) relative to that of wild-type MbCO at neutral pH (507 cm^{-1}) (*29*, *30*).

It is interesting to note that $\bar{\nu}_{Fe-NO}$ is 8 cm^{-1} higher for H93G(Im)NO than for wild-type MbNO. Removal of the covalent attachment between the protein and proximal ligand results in a change in the orientation of the ligand in the proximal pocket relative to that in the wild type, thereby affecting Fe−ligand orbital overlap and $\bar{\nu}_{Fe-NO}$. This observation will be discussed in greater detail in the context of six-coordinate H93G(L)NO bound with a variety of organic ligands (L) (*31*).

The resonance Raman data reflect differences between the five- and six-coordinate H93G single and double mutants. The five-coordinate MbNO $\bar{\nu}_{Fe-NO}$ values (ca. 535 cm^{-1}) are lower than those for the six-coordinate MbNO complexes (ca. 560 cm^{-1}), while the $\bar{\nu}_{N-O}$ values measured by FTIR are higher for the five-coordinate MbNO complexes (ca. 1670 cm^{-1}) than for the six-coordinate complexes (ca. 1613 cm^{-1}). To a first approximation, $\bar{\nu}_{Fe-NO}$ and $\bar{\nu}_{N-O}$ appear to be anticorrelated for five-coordinate compared with values for six-coordinate MbNO proteins. A plot of $\bar{\nu}_{Fe-NO}$ versus $\bar{\nu}_{N-O}$ generates a straight line with a slope of −0.38 and an *R* of 0.90, as shown in Figure 7. However, not all of the values for proteins in this study fall directly on this line; there is some scatter to the data, the origin of which is discussed below.

The detailed differences in the $\bar{\nu}_{Fe-NO}$ values for the Mb mutants presented here are not as straightforward to interpret as the differences observed in the $\bar{\nu}_{N-O}$ values. Unlike with the N−O stretching frequencies, the effect of distal mutations such as H64V is different in the wild-type background and in the H93G background. Specifically, $\bar{\nu}_{Fe-NO}$ increases by ∼3 cm^{-1} for H64V as compared with the wild type, while

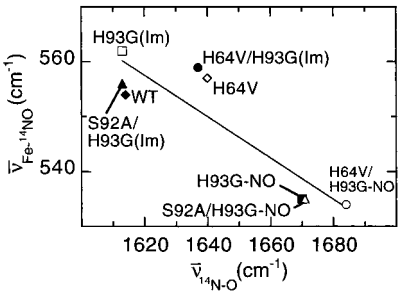

FIGURE 7: Correlation of $\bar{\nu}_{^{14}N-O}$ with $\bar{\nu}_{Fe-^{14}NO}$ for WT MbNO (◆), H64V MbNO (◇), H93G(Im)NO (□), H93G−NO (■), H64V/H93G(Im)NO (●), H64V/H93G−NO (○), S92A/H93G(Im)NO (▲), and S92A/H93G−NO (△). A linear fit to the data gives a slope of −0.38 and an *R* of 0.90.

$\bar{\nu}_{Fe-NO}$ decreases by ∼3 cm^{-1} for six-coordinate H64V/H93G compared with H93G(Im)NO, and is essentially the same for five-coordinate H64V/H93G compared with five-coordinate H93G−NO. In contrast, the H64V mutation results in a similar increase in the N−O stretching frequency for H64V compared with the wild type (26 cm^{-1}), six-coordinate H64V/H93G(Im)NO compared with H93G(Im)-NO (24 cm^{-1}), and five-coordinate H64V/H93G−NO compared with H93G−NO (14 cm^{-1}). The S92A mutation has no effect on either $\bar{\nu}_{N-O}$ for five- and six-coordinate MbNO or $\bar{\nu}_{Fe-NO}$ for the five-coordinate H93G double mutant, but S92A does affect $\bar{\nu}_{Fe-NO}$ for the six-coordinate H93G double mutant.

Unlike the N−O stretching frequency, $\bar{\nu}_{Fe-NO}$ does not appear to be a good probe for nearby electrostatic perturbations due to mutations in the distal pocket. Differences in the ability of the N−O and Fe−NO bonds to sense changes in the local electrostatic environment caused by mutations are discussed elsewhere in detail through comparison with C−O and Fe−CO bonding[2] for electrostatic mutants of Mb (*28*). In particular, $\bar{\nu}_{N-O}$ and $\bar{\nu}_{Fe-NO}$ are attributed to the projection of the local electric field within the protein onto the N−O and Fe−NO bonds. This internal Stark effect arises from both bonding and anharmonicity contributions to the Stark tuning rate $\Delta\mu$. The bent geometry of the Fe−N−O complex implies that the projection of the local electric field onto the Fe−NO and N−O bonds will differ, giving rise to differing responses of $\bar{\nu}_{N-O}$ and $\bar{\nu}_{Fe-NO}$ to changes in the electrostatic environment introduced by the heme pocket mutations. As a result, mutations that induce electrostatic changes do not lead to an apparent, quantitative correlation between $\bar{\nu}_{Fe-NO}$ values determined by resonance Raman and $\bar{\nu}_{N-O}$ values determined by FTIR. In other words, there is no apparent linear correlation between Fe−NO and N−O bond strengths, at least for the Mb mutants in this study. This finding is consistent with results reported earlier for distal mutations H64L, V68W, and V68T in which there was no apparent correlation between $\bar{\nu}_{Fe-NO}$ and $\bar{\nu}_{N-O}$ measured by resonance Raman spectroscopy (*11*). These results imply

[2] In general, $\bar{\nu}_{C-O}$ and $\bar{\nu}_{Fe-CO}$ exhibit a strong negative linear correlation with a slope of −0.82 for the plot of $\bar{\nu}_{C-O}$ versus $\bar{\nu}_{Fe-CO}$ for a variety of MbCO single mutations, which is generally attributed to π-back-bonding between Fe and CO (*11*, *20*, *28*, *32*). However, in the case of other heme proteins such as peroxidases and oxidases, $\bar{\nu}_{C-O}$ and $\bar{\nu}_{Fe-CO}$ do not exhibit a strong linear correlation due to a significant contribution from σ-donation from the *trans* axial ligand to the Fe−CO complex (*33*).

that unlike the N−O bond, the Fe−NO bond is insensitive to distal pocket mutations that perturb the electrostatic potential. However, it is possible that the Fe−NO and N−O bond strengths still may be correlated in other systems. For example, resonance Raman data for five-coordinate porphyrin Fe−NO model complexes containing a variety of electron-withdrawing and electron-donating porphyrin ring substituents show a strong negative correlation between $\bar{\nu}_{Fe-NO}$ and $\bar{\nu}_{N-O}$ (*10*). A more systematic approach to probing π-back-bonding between Fe and NO is being pursued using H93G with various organic ligands (*31*). Additional insight into π-back-bonding within the MbNO system can be obtained from direct assessment of NO binding to the H93G Mb complexes in the presence of various ligands; this is discussed in detail elsewhere (*31*).

Binding of Imidazole to Five-Coordinate MbNO Complexes. Equilibrium binding constants provide a relative measure of the imidazole affinity for binding to the five-coordinate MbNO complexes of H93G mutants. Factors that affect this affinity could be the stability of imidazole in the proximal pocket, in addition to the relative strengths of Fe−NO and Fe−ligand bonds in MbNO complexes. The S92A mutation eliminates potential hydrogen bonding between imidazole and residue 92 and increases the volume of the proximal cavity. As a result, the S92A mutation decreases the level of stabilization of imidazole in the proximal pocket, thereby leading to a lower value for K_{Im} (*24*). As expected, the V68L mutation does not directly affect the proximal pocket, and therefore has no effect on K_{Im}. However, the imidazole affinity decreases for H64V/H93G−NO compared with that for H93G−NO, implying that the distal H64V mutation does affect the affinity of the proximal imidazole ligand. It is possible that changes on the distal side of the heme pocket affect the proximal cavity. Earlier work in our lab on H93G(Im)CO and related distal and proximal double mutants suggests that distal mutations such as H64V relieve steric constraint in the distal pocket that can be translated to the proximal side of the heme pocket (*21*). This relaxation of steric packing in the heme geometry could alter the affinity of imidazole for the proximal pocket. Furthermore, two-dimensional ^{1}H NMR of H64V/H93G(Im)-CN indicates that the H64V mutation results in a change in the orientation of imidazole in the proximal pocket by 90° relative to wild-type MbCN (*21*). In the case of H64V/H93G−NO, the orientation of imidazole in the proximal pocket could change the Fe−ligand bond strength and, ultimately, the imidazole affinity for the five-coordinate MbNO complex.

Interestingly, no obvious correlation was found between the imidazole affinity and either $\bar{\nu}_{N-O}$ or $\bar{\nu}_{Fe-NO}$ for the five-coordinate H93G−NO single and double mutants. If one interprets $\bar{\nu}_{N-O}$, $\bar{\nu}_{Fe-NO}$, and K_{Im} values to be related to the bond strengths of the N−O, Fe−NO, and Im−Fe bonds, respectively, then the results presented in this paper have interesting implications for the inverse *trans* effect of NO binding to heme proteins.[3] The data suggest that the N−O, Fe−NO, and Im−Fe bonds are not correlated for Mb mutants that perturb the electrostatic potential on the distal side. If vibrational and ligand affinity data are truly related to bond strengths, then the data do not support the hypothesis of the inverse *trans* effect of NO binding in the Mb mutants presented here. Strengthening the N−O bond by introducing mutations in the heme pocket of Mb does not necessarily result in a weakening of the Fe−NO bond or a strengthening of the Fe−Im or Fe−His bond, as implied by π-back-bonding and the inverse *trans* effect of NO. Alternatively, it is possible that either K_{Im} or $\bar{\nu}_{Fe-NO}$ does not reflect the Fe−ligand or Fe−NO bond strengths, respectively. Density functional theory calculations of Fe−NO vibrational modes in porphyrin model compounds indicate that the Fe−NO stretching and Fe−N−O bending modes are mixed due to the bent geometry of Fe−NO porphyrin complexes (*10*). Mixing of the two vibrational modes could decrease the extent to which $\bar{\nu}_{Fe-NO}$ reflects the Fe−NO bond strength. Calculations indicate that the $\bar{\nu}_{Fe-NO}$ mode has an Fe−NO stretching contribution of ~65%, suggesting that this mode could still reflect the Fe−NO bond strength. However, the mixing of vibrational modes causes $\bar{\nu}_{Fe-NO}$ to depend on the Fe−N−O bond angle, a result that suggests $\bar{\nu}_{Fe-NO}$ may be affected by structural as well as electrostatic changes induced by distal pocket mutations, further complicating comparisons between $\bar{\nu}_{N-O}$, $\bar{\nu}_{Fe-NO}$, and K_{Im}. It is possible that the *trans* effect and π-back-bonding of the Fe−NO complexes hold for broad comparisons between different heme proteins, such as Mb, Hb, and sGC, although they do not hold quantitatively for Mb mutants that perturb the electrostatic environment of the heme pocket. Perhaps introducing mutations that perturb the distal pocket environment does not mimic changes in Fe−NO bonding caused by mutating the proximal ligand. We are currently studying the effects of the proximal ligand on the *trans* effect and π-back-bonding of NO using H93G bound with various organic ligands (*31*). The *trans* effect and π-back-bonding of NO in the H93G system will be discussed in more detail elsewhere in comparison with rates measured for the dissociation of NO from the H93G MbNO complexes, substituted with various organic ligands (*31*).

IR Spectra of the N−O and C−O Stretch in V68L Variants. NO stretching frequencies for the V68L−NO, six-coordinate V68L/H93G(Im)NO, and five-coordinate V68L/H93G−NO variants are presented in Figure 3 and Table 1. Unlike other variants in this study, proteins containing the V68L mutation exhibit multiple, isotope-sensitive bands in their ^{14}NO and ^{15}NO photolysis difference spectra. Comparison of six-coordinate MbNO spectra obtained at pH 5.3 and 9.0 identify the band at 1621 cm^{-1} to be a low-pH band, while the bands at 1575 and 1604 cm^{-1} are present in the pH range of 5.3−9.0. These bands appear to represent protonation substates analogous to the well-characterized protonation substates of $\bar{\nu}_{C-O}$ in MbCO (*26*). Though it is clear that the bands are pH sensitive, it is not obvious why V68L MbNO should exhibit such a pH dependence while

[3] The equilibrium constant (K_{Im}) of imidazole binding to the five-coordinate H93G−NO single and double mutants is equal to the ratio of the rates for imidazole association (k_{on}) and dissociation (k_{off}) from the five-coordinate MbNO complex (i.e., $K_{Im} = k_{on}/k_{off}$). Ideally, the $\bar{\nu}_{N-O}$ and $\bar{\nu}_{Fe-NO}$ data should be compared with the rate of imidazole dissociation from the six-coordinate H93G(Im)NO complexes of the single and double mutants to form five-coordinate MbNO. In principle, the rate of ligand dissociation from the six-coordinate H93G(Im)NO complexes can be measured by monitoring changes in the Soret band absorption following stopped-flow dilution of six-coordinate samples into buffer containing no imidazole. However, we have found that imidazole dissociation from six-coordinate H93G−NO occurs during the mixing time of the stopped-flow apparatus (~5 ms), preventing the accurate determination of k_{off} for imidazole to compare with $\bar{\nu}_{N-O}$ and $\bar{\nu}_{Fe-NO}$ (data not shown).

other mutants do not. These bands may arise from changes in the distal pocket geometry due to the introduction of a slightly larger hydrophobic residue at position 68. Residue 68 has been shown to be quite sensitive to mutation, particularly the electrostatic mutations such as Asp, Glu, and Asn that dramatically affect $\bar{\nu}_{N-O}$ and NO rebinding rates for MbNO (*20*, *34*). Similarly, substitution of Val 68 with large hydrophobic residues, such as Phe and Trp, causes significant changes in diatomic ligand rebinding and dissociation rates (*27*, *35*). Moreover, crystal structures of V68L indicate that Leu substitution at residue 68 causes significant changes in the Mb distal pocket environment, even though leucine is only slightly larger than valine (*35*). X-ray crystal structures of the met H_2O and deoxy forms of the V68L single mutant indicate that this mutation excludes the unligated water molecule usually present in the distal pocket of met H_2O and deoxy WT Mb (*35*). It is possible that structural changes due to the V68L mutation could also occur in MbNO. Such changes could alter the pK_a of neighboring distal pocket residues, giving rise to protonation substates of distal pocket residues that result in changes in $\bar{\nu}_{N-O}$ for V68L MbNO relative to WT MbNO.

The unexpected observation of apparent pH-sensitive bands in the FTIR photolysis difference spectra for V68L and V68L/H93G MbNO samples led us to compare the FTIR spectra for the CO-bound forms of the V68L mutants. The vibrational spectra of MbCO have been characterized extensively for a large number of mutants, leading to a detailed understanding of the effect of distal pocket mutations on $\bar{\nu}_{C-O}$ (*26*, *27*, *36*, *37*). In an attempt to direct attention toward the unusual MbNO spectra of the V68L mutants and to gain insight about possible effects of the V68L mutation on the conformational substates of the protein, we examined both room-temperature absorption and cryogenic photolysis difference spectra for V68L−CO and V68L/H93G(Im)CO. As reported previously, the room-temperature absorption spectrum of V68L MbCO is very similar to that of wild-type MbCO (Figure 5) (*27*). The similarity in $\bar{\nu}_{C-O}$ values is reasonable since substitution of valine with leucine is not anticipated to alter the local electrostatic environment of the distal pocket.

In contrast to the room-temperature $\bar{\nu}_{C-O}$ data, the cryogenic photolysis difference spectra do not resemble the room-temperature spectra, particularly for the V68L mutant (Figure 5). Vibrational spectra of MbCO have been shown to vary significantly with decreasing sample temperature (*26*, *36*). In human wild-type Mb, the area of the A_0 band increases moderately with respect to that of the A_1 band when the temperature is decreased (*36*). As depicted in Figure 5, the A_0 band of wild-type sperm whale MbCO is also observed to increase for spectra at 74 K relative to room temperature. A similar shift from the A_1 to the A_0 substate occurs in wild-type MbCO when the solution pH is decreased due to protonation of the distal His 64 residue (*26*, *36*, *37*). In striking contrast to the moderate difference between room-temperature and cryogenic IR spectra of wild-type MbCO, the photolysis difference spectrum of V68L MbCO is dramatically distinct from the corresponding room-temperature spectrum. Unlike the moderate temperature dependence exhibited by the wild-type MbCO spectra, spectra for V68L−CO indicate that a majority of the protein shifts from the A_1 (1941 cm^{-1}) to the A_0 (1964 cm^{-1}) substate when the temperature is decreased. The dramatic temperature effect observed for the V68L and V68L/H93G MbCO spectra implies that this mutation has a large and unanticipated effect on the distal pocket environment. It is possible that the larger, flexible leucine side chain could adopt additional conformations that perturb the position of the distal histidine, allowing alternative conformations to dominate at low temperatures for V68L compared with wild-type MbCO.

Additionally, the pH dependence of MbCO spectra for the V68L mutants differs from that reported earlier for wild-type MbCO (Figure 4) (*26*). For wild-type and H93G(Im) MbCO, the A_1 substate (1945 cm^{-1}) dominates the spectrum at pH 7.0. As the pH is decreased to 5.3, only ~30% of the A_1 substate MbCO species is converted to the A_0 substate (1965 cm^{-1}) in wild-type MbCO. Although the A_1 substate (1941 cm^{-1}) dominates the V68L and V68L/H93G(Im) MbCO spectra at pH 9.0, it is completely converted to the A_0 substate (1962 cm^{-1}) when the pH is reduced to 7.0, particularly for the V68L double mutant. At pH 5.3, MbCO spectra of V68L and V68L/H93G are completely dominated by the A_0 substate (1962 cm^{-1}) with only a small band at 1931 cm^{-1}. The V68L mutation clearly affects the temperature dependence and pH sensitivity of $\bar{\nu}_{C-O}$ bands in MbCO, altering the distribution of protein species in the A_1 and A_0 substates, suggesting that this mutation affects pK_a values of titratable residues present in the distal pocket of Mb, such as His 64. Typically, the A_0 substate of MbCO has been associated with protonation of His 64 that causes the residue to rotate away from the bound CO, thereby decreasing the level of electrostatic interaction between CO and the distal histidine (*38*). The CO spectra presented here imply that the distal His 64 is protonated near neutral, rather than acidic, pH. The unusual pH dependence of $\bar{\nu}_{C-O}$ observed for V68L−CO and V68L/H93G(Im)CO is not unlike the atypical observations of $\bar{\nu}_{N-O}$ for the NO-bound forms of these proteins (i.e., spectra that are very different from that of wild-type MbNO). The observation of unusual pH effects in both MbCO and MbNO spectra for V68L and V68L/H93G suggests that the V68L mutation changes the distal pocket environment. This mutation may affect the pK_a of nearby residues in the distal pocket, thereby inducing an electrostatic effect not anticipated from the Val to Leu mutation itself.

SUMMARY

FTIR spectroscopy of NO-bound distal and proximal H93G double mutants indicates that $\bar{\nu}_{N-O}$ is affected by distal, but not proximal, mutations that alter the electrostatic environment of the heme pocket. The results imply that NO binds on the distal side of five- and six-coordinate H93G. Resonance Raman spectroscopy of the MbNO mutants suggests that $\bar{\nu}_{Fe-NO}$ is not sensitive to mutations that alter distal pocket electrostatics, leading to only a qualitative comparison between $\bar{\nu}_{N-O}$ and $\bar{\nu}_{Fe-NO}$. The affinity of imidazole binding to five-coordinate H93G−NO was found to vary for the distal and proximal H93G double mutants. However, the equilibrium binding constant, K_{Im}, does not correlate well with either $\bar{\nu}_{N-O}$ or $\bar{\nu}_{Fe-NO}$, implying that mutations that alter the electrostatic environment of the heme pocket do not probe the inverse *trans* effect or π-backbonding of NO binding to heme proteins such as Mb.

ACKNOWLEDGMENT

The strategy of probing the NO binding location in H93G was based on a similar strategy designed by Robert B. Hu to address CO binding in H93G (*21*). We are also grateful to Eun Sun Park for her expert assistance in collecting and analyzing the resonance Raman data presented in this paper. The FTIR instrument used for this work is located at the Stanford FEL Center supported by the Air Force Office of Scientific Research (Grant F49620-00-1-0349).

REFERENCES

1. Polizio, F., De Sanctis, G., Ascenzi, P., and Coletta, M. (1998) *J. Biol. Inorg. Chem. 3*, 458−462.
2. Ascenzi, P., Coletta, M., Desideri, A., and Brunori, M. (1985) *Biochim. Biophys. Acta 829*, 299−302.
3. Taketa, F., Antholine, W. E., and Chen, J. Y. (1978) *J. Biol. Chem. 253*, 5448−5451.
4. Henry, Y., and Banerjee, R. (1973) *J. Mol. Biol. 73*, 469−482.
5. Yonetani, T., Tsuneshige, A., Zhou, Y., and Chen, X. (1998) *J. Biol. Chem. 273*, 20323−20333.
6. Zhao, Y., Brandish, P. E., Ballou, D. P., and Marletta, M. A. (1999) *Proc. Natl. Acad. Sci. U.S.A. 96*, 14753−14758.
7. Stone, J. R., Sands, R. H., Dunham, W. R., and Marletta, M. A. (1995) *Biochem. Biophys. Res. Commun. 207*, 572−577.
8. Stone, J. R., and Marletta, M. A. (1994) *Biochemistry 33*, 5636−5640.
9. Yu, A. E., Hu, S., Spiro, T. G., and Burstyn, J. N. (1994) *J. Am. Chem. Soc. 116*, 4117−4118.
10. Vogel, K. M., Kozlowski, P. M., Zgierski, M. Z., and Spiro, T. G. (1999) *J. Am. Chem. Soc. 121*, 9915−9921.
11. Tomita, T., Hirota, S., Ogura, T., Olson, J. S., and Kitagawa, T. (1999) *J. Phys. Chem. B 103*, 7044−7054.
12. Barrick, D. (1994) *Biochemistry 33*, 6546−6554.
13. Decatur, S. M., Franzen, S., DePillis, G. D., Dyer, R. B., Woodruff, W. H., and Boxer, S. G. (1996) *Biochemistry 35*, 4939−4944.
14. Pond, A. E., Roach, M. P., Sono, M., Rux, A. H., Franzen, S., Hu, R., Thomas, M. R., Wilks, A., Dou, Y., Ikeda-Saito, M., Ortiz de Montellano, P. R., Woodruff, W. H., Boxer, S. G., and Dawson, J. H. (1999) *Biochemistry 38*, 7601−7608.
15. Roach, M. P., Pond, A. E., Thomas, M. R., Boxer, S. G., and Dawson, J. H. (1999) *J. Am. Chem. Soc. 121*, 12088−12093.
16. Barrick, D. (1995) *Curr. Opin. Biotechnol. 6*, 411−418.
17. Decatur, S. M., and Boxer, S. G. (1995) *Biochemistry 34*, 2122−2129.
18. Decatur, S. M., DePillis, G. D., and Boxer, S. G. (1996) *Biochemistry 35*, 3925−3932.
19. Thomas, M. R., and Boxer, S. G. (2001) *Biochemistry 40*, 8588−8596.
20. Park, E. S., Thomas, M. R., and Boxer, S. G. (2000) *J. Am. Chem. Soc. 122*, 12297−12303.
21. Hu, R. (1999) Ph.D. Thesis, Stanford University, Stanford, CA.
22. DePillis, G. D., Decatur, S. M., Barrick, D., and Boxer, S. G. (1994) *J. Am. Chem. Soc. 116*, 6981−6982.
23. Yonetani, T., Yamamoto, H., Erman, J. E., Leigh, J. S., and Reed, G. H. (1972) *J. Biol. Chem. 247*, 2447−2455.
24. Decatur, S. M., Belcher, K. L., Rickert, P. K., Franzen, S., and Boxer, S. G. (1999) *Biochemistry 38*, 11086−11092.
25. Miller, L. M., Pedraza, A. J., and Chance, M. R. (1997) *Biochemistry 36*, 12199−12207.
26. Müller, J. D., McMahon, B. H., Chien, E. Y. T., Sligar, S. G., and Nienhaus, G. U. (1999) *Biophys. J. 77*, 1036−1051.
27. Li, T., Quillin, M. L., Phillips, G. N., and Olson, J. S. (1994) *Biochemistry 33*, 1433−1446.
28. Park, E. S., and Boxer, S. G. (2001) *J. Am. Chem. Soc.* (submitted for publication).
29. Ramsden, J., and Spiro, T. G. (1989) *Biochemistry 28*, 3125−3128.
30. Vogel, K. M., Kozlowski, P. M., Zgierski, M. Z., and Spiro, T. G. (2000) *Inorg. Chim. Acta 297*, 11−17.
31. Thomas, M. R., Brown, D., Franzen, S., and Boxer, S. G. (2001) (manuscript in preparation).
32. Phillips, G. N., Teodoro, M. L., Li, T., Smith, B., and Olson, J. S. (1999) *J. Phys. Chem. B 103*, 8817−8829.
33. Franzen, S. (2001) *J. Am. Chem. Soc.* (submitted for publication).
34. Petrich, J. W., Lambry, J.-C., Balasubramanian, S., Lambright, D. G., Boxer, S. G., and Martin, J. L. (1994) *J. Mol. Biol. 238*, 437−444.
35. Quillin, M. L., Li, T., Olson, J. S., Phillips, G. N., Dou, Y., Ikeda-Saito, M., Regan, R., Carlson, M., Gibson, Q. H., Li, H., and Elber, R. (1995) *J. Mol. Biol. 245*, 416−436.
36. Balasubramanian, S., Lambright, D. G., and Boxer, S. G. (1993) *Proc. Natl. Acad. Sci. U.S.A. 90*, 4718−4722.
37. Braunstein, D. P., Chu, K., Egeberg, K. D., Frauenfelder, H., Mourant, J. R., Nienhaus, G. U., Ormos, P., Sligar, S. G., Springer, B. A., and Young, R. D. (1993) *Biophys. J. 65*, 2447−2454.
38. Yang, F., and Phillips, G. N. (1996) *J. Mol. Biol. 256*, 762−774.
39. Park, E. S., Andrews, S. S., Hu, R. B., and Boxer, S. G. (1999) *J. Phys. Chem. B 103*, 9813−9817.
40. Andrews, S. S., and Boxer, S. G. (2000) *Rev. Sci. Instrum. 71*, 3567−3569.

BI011440L